Journal of Nanobiotechnology

RESEARCH Open Access

Temporal and spatial resolution of magnetosome degradation at the subcellular level in a 3D lung carcinoma model

Alicia G. Gubieda[1*], Lucía Gandarias[1,2], Mihály Pósfai[3,4], Ajith Pattammattel[5], M. Luisa Fdez-Gubieda[6], Ana Abad-Díaz-de-Cerio[1*] and Ana García-Prieto[7*]

Abstract

Magnetic nanoparticles offer many exciting possibilities in biomedicine, from cell imaging to cancer treatment. One of the currently researched nanoparticles are magnetosomes, magnetite nanoparticles of high chemical purity synthesized by magnetotactic bacteria. Despite their therapeutic potential, very little is known about their degradation in human cells, and even less so of their degradation within tumours. In an effort to explore the potential of magnetosomes for cancer treatment, we have explored their degradation process in a 3D human lung carcinoma model at the subcellular level and with nanometre scale resolution. We have used state of the art hard X-ray probes (nano-XANES and nano-XRF), which allow for identification of distinct iron phases in each region of the cell. Our results reveal the progression of magnetite oxidation to maghemite within magnetosomes, and the biosynthesis of magnetite and ferrihydrite by ferritin.

*Correspondence:
Alicia G. Gubieda
alicia.gascon@ehu.eus
Ana Abad-Díaz-de-Cerio
ana.abad@ehu.eus
Ana García-Prieto
ana.garciap@ehu.eus

Full list of author information is available at the end of the article

Graphical Abstract

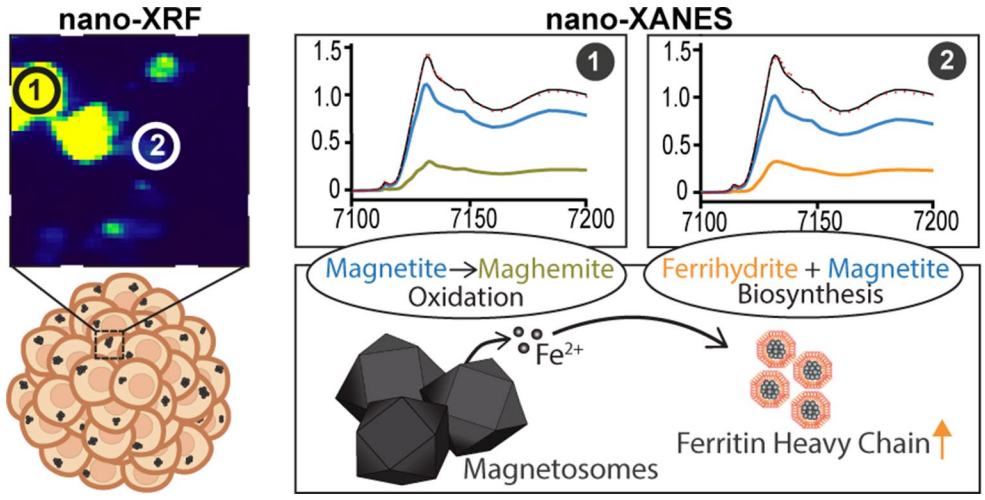

Keywords Magnetosome, Magnetic nanoparticle degradation, Ferritin, Biomineralisation, Nano-XANES,

Cancer has become one of the leading causes of premature death worldwide, with the number of cases expected to increase to 28.4 million by 2040 [1]. Amongst all cancers, lung cancer stands out as the deadliest, with a mortality rate (18%) that surpasses those of breast, prostate and colorectal cancers combined. Its poor overall survival rates are mainly associated with late diagnosis, resistance to common treatments like chemo and radiotherapy, and the toxic side effects associated with conventional therapies [2], highlighting the need for innovative approaches to cancer diagnosis and treatment. In response to these challenges, nanotechnology has emerged as a promising avenue.

Amongst the new nanotechnologies of interest, iron oxide magnetic nanoparticles (IONPs) are promising candidates. Due to their magnetic properties, IONPs can be directed to the region of interest using an external magnetic field, thus avoiding damage to healthy tissues. Their physicochemical properties allow for multiple applications, from magnetic resonance imaging for diagnostic purposes [3, 4], to magnetogenetics [5], photothermia [6] and magnetic hyperthermia [7] cancer treatments. Furthermore, IONPs can be administered via inhalation to target lung tumours [8]. While most nanoparticles are still in a preclinical stage, some IONPs have been approved for glioblastoma treatment in Europe since 2010 [9], and there are clinical trials in progress for their use in prostate carcinoma in the USA [10] and pancreatic ductal adenocarcinoma in Spain [11].

Obtaining uniform nanoparticles of a similar mean particle size and uniform crystallinity is often a challenge with chemically synthesized nanoparticles. One promising alternative are magnetosomes, nanoparticles of high chemical purity synthesized by magnetotactic bacteria [12–14]. Magnetosomes are biocompatible and surrounded by a proteolipidic membrane, allowing for modifications with drugs, peptides and antibodies [15–18]; they have a mineral core of high purity composed of either magnetite (Fe_3O_4) or greigite (Fe_3S_4); and present a very narrow size distribution, which ranges from 30 to 120 nm depending on the bacterial species [12, 19].

While the biocompatibility and heating potential of magnetosomes have been well documented [20–22], very little is known about their transformation and degradation process once they are inside living organisms. Since iron is naturally present in human cells, magnetosomes are expected to be degraded and easily incorporated into the patient's metabolism. Understanding how they degrade in tumours is particularly relevant for their use in nanomedicine, as it might reveal insights into the durability of magnetosomes as therapeutic agents both in their role as heat generators for hyperthermia and as Fe^{2+} generating agents for ferroptosis induction [6], and on unknown aspects of iron metabolism. Additionally, tumours present characteristics [Reviewed in 23] that affect their interaction with drugs and nanoparticles (NPs), and are replicable in three-dimensional tumour models: lack of oxygen in the interior of the tumour; variation in the cell's energy metabolism; acidic microenvironment; cell-cycle arrest in the interior of the tumour and lastly, tight interactions between cells. These characteristics can affect the degradation process of IONPs: tight cell interactions could affect nanoparticle excretion, the acidic microenvironment could accelerate degradation, while the cell-cycle arrest could slow down the degradation process. Moreover, the degradation of

magnetosomes within cancer cells could hold therapeutic potential, as the release of iron ions can stimulate the production of reactive oxygen species (ROS) through Fenton and Fenton-like reactions, inducing lipid peroxidation and ferroptosis [24].

A few studies have been carried out on IONP degradation: in vivo studies in mice and rats have shown that nanoparticles are internalized by the liver and spleen, and then slowly degraded by them [25–28]. The rate of degradation is highly affected by factors such as the coating of the nanoparticles, their hydrodynamic size, and their internal architecture [27]. The degradation of magnetosomes is of particular interest, given their therapeutic potential [29]. Some studies have been done on this topic: our group previously detailed the magnetosome degradation process in RAW264.7 macrophages and A549 human lung carcinoma cells in two-dimensional cultures. We observed both excretion to the surrounding environment and intracellular degradation, producing maghemite, ferrihydrite and goethite [30]. Meanwhile, another group has analysed magnetosome degradation by mesenchymal stem cells, showing a remagnetisation process in two-dimensional (2D) stem cell cultures that they suggest could be stem cell and 2D culture specific [31].

In this work, we present evidence on the degradation process of magnetosomes at the subcellular level in a 3D human lung carcinoma model for a 36-day period, using magnetosomes isolated from *Magnetospirillum gryphiswaldense*. We have used cutting-edge synchrotron probes (nano X-Ray Fluorescence combined with nano X-Ray Absorption Near Edge Structure) to map the distinct iron phases appearing upon degradation with nanometer scale resolution, demonstrating the potential of this technique to trace chemical phases at the subcellular level. We have combined these data with TEM, magnetometry and gene expression analysis, to provide new insights on both magnetosome degradation, and on the biosynthesis of magnetic nanoparticles by a human lung carcinoma tumour model.

Results and discussion

Microscopy analysis of magnetosome incorporation and degradation in a 3D human lung carcinoma model

To study magnetosome degradation in a human lung carcinoma model, magnetosomes were isolated from *Magnetospirillum gryphiswaldense* and then incubated for 2 h with A549 human lung carcinoma cells. The magnetosome-loaded cells were used to generate 3D spheroids, which were kept and studied for up to 36 days. We first confirmed and quantified iron internalisation by means of SQUID magnetometry, which revealed an internalized amount of approximately 26 pg of magnetite per cell (Figure S1A-B). We also confirmed that this amount of iron was not toxic for the spheroids by measuring cell activity (ATP quantification) 10 days after magnetosome internalisation (Figure S1C).

We then proceeded to visualize magnetosome internalisation and degradation via transmission electron microscopy (TEM) image acquisition (Fig. 1). Images were acquired from spheroids sections of 70 nm in width, and samples were not stained with osmium or uranyl acetate, as these can generate small dark dots, which could be confused with magnetosome degradation products [32]. Magnetosomes were visible mostly in clusters, which were present for the entire analysed period, from the earliest time point imaged (2 h), to the last time point (36 days) (magnetosomes marked in blue in Fig. 1A). A change in magnetosome size (≈44 nm in diameter at the starting point) was visible from two days after internalisation. The decrease in size persisted in time, reaching the lowest average diameter of 30 nm by 20 days of degradation (Fig. 1B). The degradation of magnetosomes seemed to halt towards the end of the analysed period, which could be due to the cell-cycle arrest characteristic of the interior of 3D tumour models. While lack of staining prevented the visualisation of intracellular membranes in our samples, previous reports indicate that clusters of magnetosomes are located in endosomes/lysosomes [33].

Moreover, from two days after internalisation onwards, smaller nanoparticles were visible, with diameters ranging from 2 to 10 nm (Fig. 1A). These nanoparticles were present both scattered all over the cell and in clusters, often nearby areas in which magnetosomes were also visible. Previous studies on IONP degradation [34] have shown that similar clustered small nanoparticles are enclosed inside membranes (i.e., in endosomes or lysosomes), suggesting that the nanoparticles we observe in clusters could be located in such organelles, while the nanoparticles scattered over the cell might be located in the cytoplasm. Due to the size range observed for these small nanoparticles (<10 nm), we hypothesized that they could be synthesized by ferritin. Ferritin is an iron storage and homeostasis protein consisting of heavy and light chain subunits, which assemble in a nano-cage with an outer diameter of 12 nm [35] and an inner cage diameter of 10 nm. Ferritin can capture highly toxic free Fe^{2+}, and store it in a mineral core of ferrihydrite.

Interestingly, the size of the small nanoparticles evolved during the degradation process, and was different for the nanoparticles found in clusters and for those dispersed (Fig. 1C). At the earlier stages (t=2 days) these nanoparticles had a diameter of 4.7 nm. However, 8 days after magnetosome internalisation, the size of the small nanoparticles increased considerably, reaching a diameter of 6.1±1.0 nm for those dispersed, and a significantly larger diameter of 8.0±1.2 nm for those found in clusters. The diameter then decreased slightly by 20 days

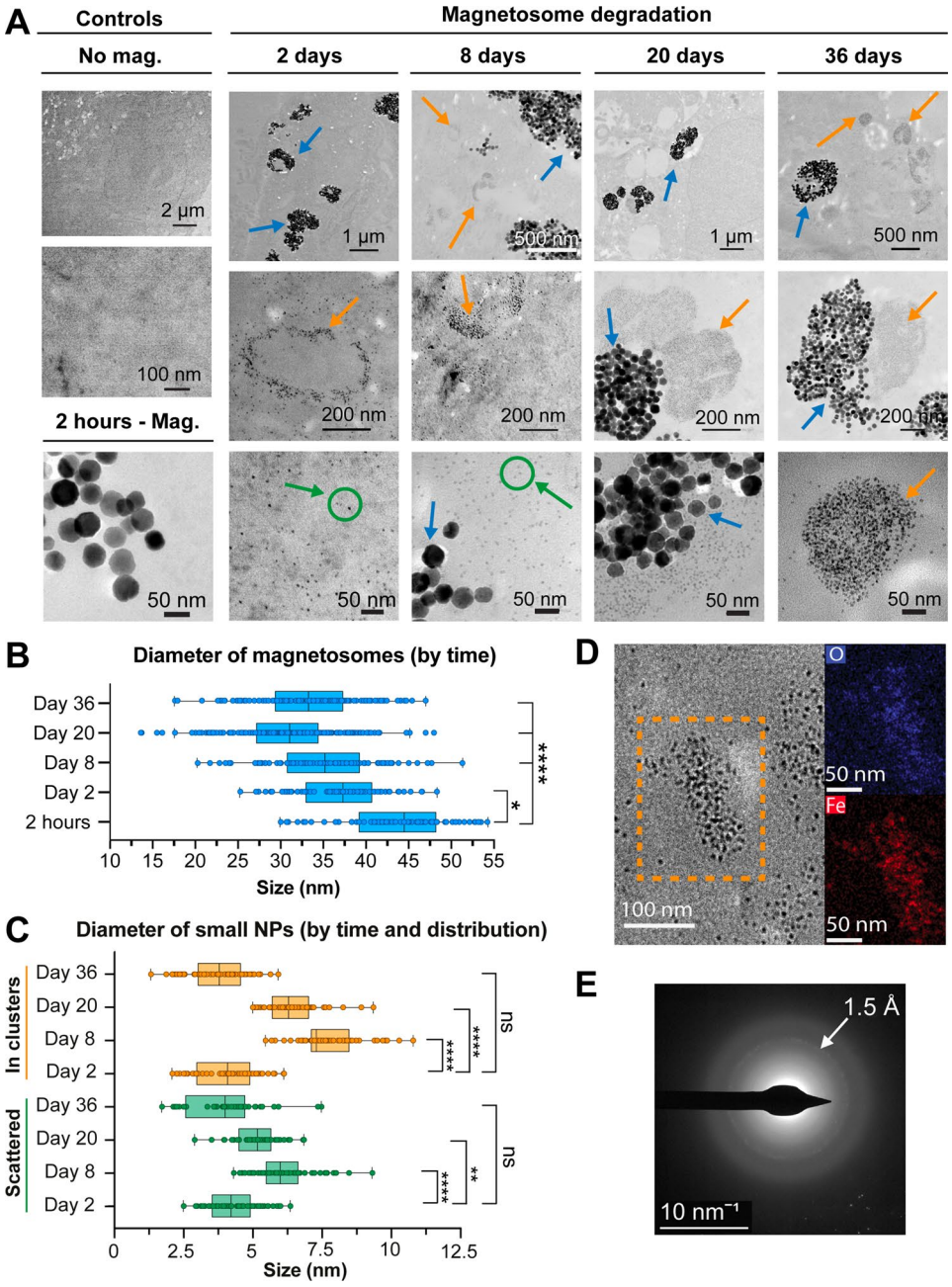

Fig. 1 **(A)** TEM images of A549 spheroid sections, incubated with magnetosomes for up to 36 days. A control of a spheroid with no magnetosomes, after 20 days of incubation, is also shown. Blue arrows point to clusters of magnetosomes. Orange arrows point to clusters of smaller NPs. Small NPs are also visible dispersed in the cell (circle in green). **(B)** Size of magnetosomes by time of degradation. **(C)** Size of smaller nanoparticles, by distribution and by time of degradation. **(D)** TEM image of a small nanoparticle cluster, 2 days after internalisation, and iron and oxygen element maps of the same region. **(E)** SAED pattern obtained from a cluster of small particles from a 20 day sample, showing a distinct ring near 1.5 Å

after magnetosome internalisation, at 5.2±0.8 nm (dispersed small NPs) and 6.4±0.9 nm (in clusters). By the final point imaged (t=36 days), these nanoparticles had regressed to their initial size, with diameters of 4.7±1 and 4.2±0.7 nm respectively.

To determine the nature of these small nanoparticles we analysed them with elemental mapping/energy dispersive X-ray spectrometry (EDS) (Fig. 1D), a method that identifies the elements present in a sample by analysing the characteristic X-rays generated by the material when it is impacted by the high energy electron beam of an electron microscope. We observed a clear enrichment in iron and oxygen in the regions containing clusters of small nanoparticles, suggesting the nanoparticles were products of magnetosome degradation. We also analysed the electron diffraction patterns of these small

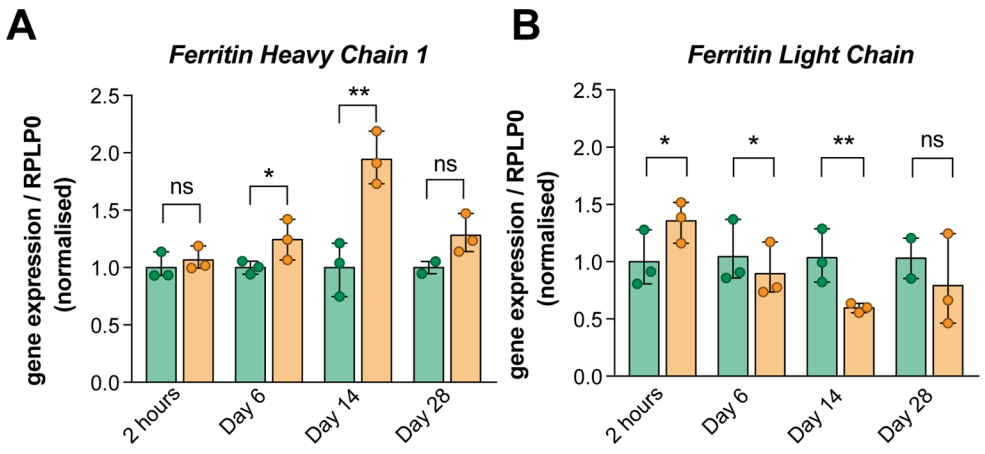

Fig. 2 Relative expression of *Ferritin Heavy Chain 1* (**A**) and *Ferritin Light Chain* (**B**) genes. Gene expression was measured at each timepoint in spheroids with magnetosomes (orange) and without magnetosomes (green), and normalised to the expression of the reference gene RPLP0

nanoparticle clusters with selected area electron diffraction (SAED) (Fig. 1E), and in some cases observed a diffuse ring around 1.5 Å. This ring suggests that some nanoparticles are on their way to developing some short-range order, whereas other clusters appeared to be entirely amorphous (they did not produce any rings in SAED patterns). The 1.5 Å ring matches that reported for ferrihydrite, the mineral core found within ferritin [36]; however the other characteristic spacing of 2-line ferrihydrite at 2.5 Å was not observed. High resolution TEM (HR-TEM) images obtained from the small nanoparticles did not show crystallinity.

We also analysed the expression of the two ferritin genes, Ferritin Heavy Chain 1 (FTH1) and Ferritin Light Chain (FTL) (Fig. 2). FTH1 encodes the heavy chain of ferritin, this subunit has ferroxidase activity [37] and can oxidize Fe^{2+} to Fe^{3+} to protect the cell from oxidative stress and inhibit ferroptosis [38]. We observed a significant increase in FTH1 expression throughout magnetosome degradation, with an expression peak halfway through the analysed period and a return to baseline towards the end (Fig. 2A), correlating with the pattern observed for the small nanoparticle diameter. This further suggests that the observed small nanoparticles are being synthesized by ferritin, and points to a different need for protection from oxidative stress at different time points of magnetosome degradation.

Interestingly, when we analysed the expression of the Ferritin Light Chain gene (FTL), we observed an initial increase in its expression at the 2 h time point, followed by a decrease in its expression with an opposing pattern to that observed for the FTH1 gene (Fig. 2B). The Light subunit of ferritin is thought to support the nucleation (crystal formation) within ferritin, although its role is still not well understood. Tissues involved in iron storage (such as the liver and spleen) are known to contain mainly FTL, as this subunit can store more iron [39]. L-rich ferritins have been reported to have a mineral core of more pronounced crystallinity [40], thus the H-enrichment we observe could be a contributing factor to the nanoparticles not having crystalline order (Fig. 1E).

Given the regression to baseline in ferritin expression (Fig. 2) and the decrease in the size of the small NPs (Fig. 1C) towards the end of the 36 day study, we considered two hypotheses: (1) that cells could be expelling iron, thereby decreasing the amount of free Fe^{2+} in the cell that needs to be captured and stored in ferritin; or (2) that a lower rate of magnetosome degradation (in the form of Fe^{2+} release from the magnetosomes) could decrease the requirement for its capture and storage in ferritin.

Iron can be expelled from the cell via ferroportin, a transmembrane protein that can transport free Fe^{2+} and is the sole known iron exporter in vertebrates [41]; or as the ferrihydrite within ferritin, as the ferritin located within lysosomes has previously been reported to be secreted through a non-classical lysosomal secretion pathway or via secretory autophagy [42, 43]. To rule out the presence of these iron secretion pathways we analysed the amount of total iron in spheroids during the 36 day period using Inductively Coupled Plasma Atomic Emission Spectroscopy (ICP/AES). This method revealed an amount of iron of around 22 pg/cell (Figure S2), which was constant throughout the experiment, indicating no iron was being lost from the spheroid. Furthermore, we performed quantitative reverse transcription PCR (qRT-PCR) to analyse the expression of ferroportin in spheroids, but the expression levels were too low to detect, suggesting that ferroportin does not play a significant role in the degradation of magnetosomes or in iron homeostasis in human lung carcinoma spheroids. These results rule out iron secretion from the lung carcinoma model, and vastly differ from those observed for magnetosome degradation

in two-dimensional cultures of human lung carcinoma cells [30]. This may be explained by the following characteristics of 3D models vs. traditional cell-culture models: cell-cell interactions lower the cells' ability to divide and split magnetosomes between daughter cells, cell-cell interactions may also decrease the ability of cells to expel magnetosomes to the surrounding media, and lower access to nutrients by cells inside the spheroid decrease their cell activity perhaps leading to a lower degradation rate of the magnetosomes within the cells. This lower access to nutrients may also affect different aspects of the cells' metabolism, including iron metabolism, as transition into 3D cultures has been shown in ovarian cancer to be associated with modifications of the iron metabolism aimed at preventing the accumulation of free and redox iron [44].

Having ruled out iron secretion from the cell, we concluded that magnetosome degradation occurs mainly in the first days after internalisation, and that the degradation rate decreases a few weeks after internalisation, perhaps due to the lower cell activity found in 3D tumour models. Lastly, we concluded that one of the products of degradation is small nanoparticles that appear to be synthesized by ferritin, and that often localise in clusters nearby magnetosomes.

Macroscopic analysis of magnetosome degradation products with XANES and magnetometry

To analyse the changes around the iron atoms during degradation, we measured the X-ray absorption near-edge structure (XANES) spectra at the Fe K-edge (Fig. 3) from the magnetosome-loaded spheroids, in BM23 Beamline of the ESRF synchrotron (France).

XANES spectra provide information about the electronic and structural organisation around the Fe absorbing atoms, and are very sensitive to the oxidation state of the absorbing atom. Several regions of the spectrum can be distinguished (Fig. 3A): (1) the pre-edge region, which appears 15–20 eV before the main edge, and depends on the nature and symmetry of the absorbing atom; (2) the edge position, which provides information on the oxidation state of the absorbing atom; and (3) the post-edge region, which gives information on the medium range order around the absorbing atom.

While we did not detect changes in the pre-edge region (Fig. 3A), we observed changes both in the edge (Fig. 3B)

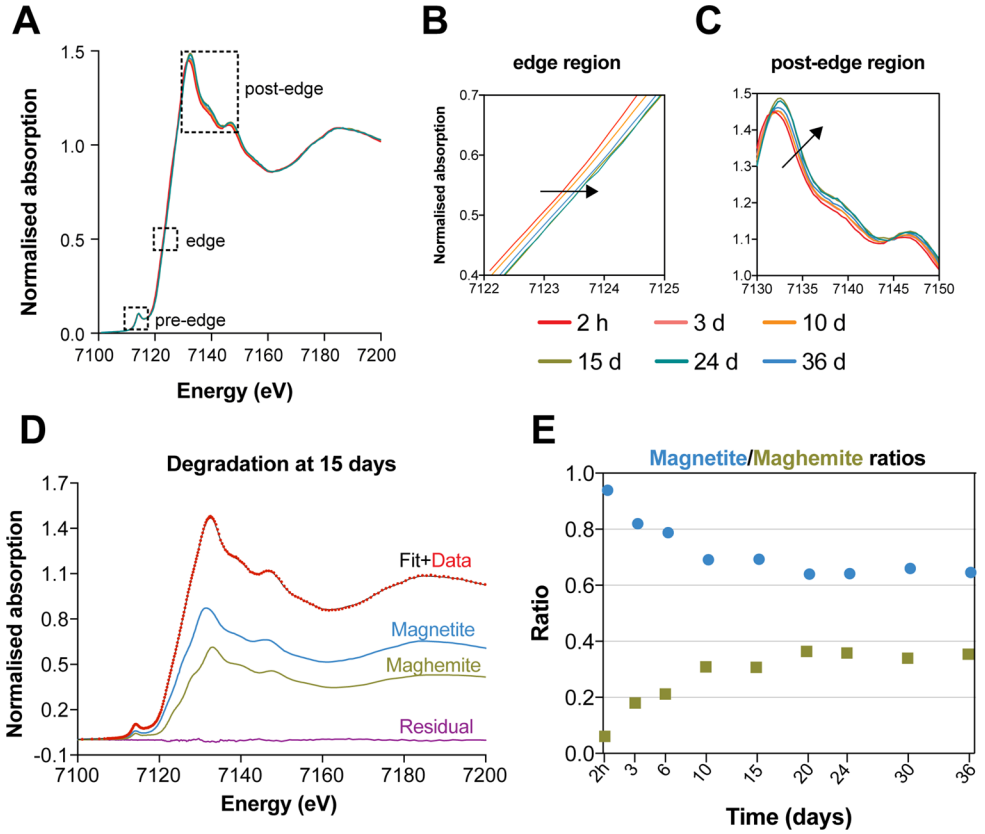

Fig. 3 **A**. Fe K-edge XANES spectra of A549 spheroids incubated with magnetosomes, from 2 h to 36 days. The pre-edge, edge, and post-edge regions are indicated with a dashed square. **B**-**C**. Zoomed up sections of the edge and post-edge regions. Shifts are shown with arrows. **D**. Linear combination fitting of sample containing spheroids with magnetosomes, 15 days after internalisation. **E**. Atomic fraction of maghemite and magnetite in spheroid samples incubated with magnetosomes, from 2 h to 36 days. Best fits contain magnetite (blue circles) and maghemite (green squares)

and post-edge regions (Fig. 3C). As shown in Fig. 3B, the edge region shifts towards higher energy during the degradation process. Similarly, the post-edge region (Fig. 3C) changes during the degradation process.

These changes to the XANES spectra suggest changes in the Fe oxidation state and in the surroundings of the Fe atoms during the degradation process. To identify the iron species appearing upon degradation, we performed a linear combination fit of our spectra at each time point to the following known standards: magnetite, maghemite, and horse spleen ferritin (with a ferrihydrite core). Results of the fits are shown in (Fig. 3D-E). Main changes occur during the first 10 days after internalisation, with the magnetite in the magnetosomes slowly oxidising into maghemite, and maghemite taking up to 36% of the iron of the cell. After this point, degradation reaches a plateau, and the best fit does not change, with the ratio of magnetite and maghemite in the sample staying the same for the rest of the analysed period. The lack of ferrihydrite in the fitting analysis of the spheroids was particularly interesting, as clusters of small NPs, which we presumed to be ferritin, were observed in the samples analysed by TEM and associated to an increase in FTH1 expression. This suggests that the contribution of other iron species, such as ferrihydrite, to the XANES spectra should be less than 10% of the total Fe in the sample [13].

Given that the magnetic properties of magnetosomes are what makes them of interest for therapeutic applications, we wondered what the effect of magnetite degradation could be on the magnetic properties of the human lung carcinoma spheroids. We employed SQUID magnetometry to measure the magnetic moment for spheroids from 1 to 36 days of degradation (Figure S3). Up to seven replicates were measured for each time point. Magnetisation overall decreased only slightly during the process, with 5% lower magnetisation at the 36 day time point compared to the starting time point. This result matches what would be expected from the XANES results, as maghemite, the main degradation product, is also ferrimagnetic, and the decrease in saturation magnetic moment expected from 35% maghemite/65% magnetite would be of 6%, given the corresponding saturation magnetisation values (92 emu/g for magnetite and 76 emu/g for maghemite).

We also measured the zero field cooled (ZFC) magnetisation curve (Fig. 4A), an experiment in which the sample in a demagnetized state is cooled down from 300 K to 10 K, and the magnetisation curve is measured while increasing temperature with an applied magnetic field of 50 Oe. This measurement is very sensitive to magnetic changes arising from the different magnetic phases present in the sample. Interestingly, the ZFC magnetisation curve does show important changes upon degradation, which are especially evident in the derivatives of the ZFC magnetisation curves (Fig. 4B). At 2 h the derivatives display mainly two peaks: one (at approx 25 K), usually attributed to surface effects, and another one (at approx 90 K) corresponding to the Verwey transition characteristic of magnetite. The latter disappears upon degradation, evidencing its sensitivity to the chemical purity of magnetite [45]. Noticeably, a shoulder can be hinted already at day 4, at around 15 K. This shoulder progressively evolves and becomes a sharp peak by day 32. This peak could be attributed to the appearance of magnetic nanoparticles emerging during the degradation process.

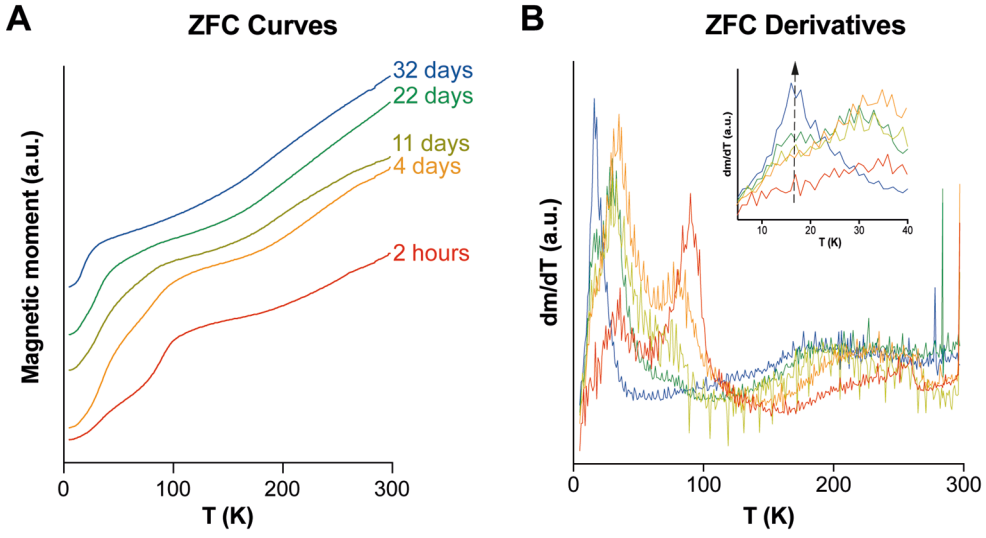

Fig. 4 **A**. Evolution of ZFC curves of A549 cell spheroids from 2 h to 32 days after magnetosome internalisation. **B**. Derivatives of ZFC magnetisation curves (shown in A) as a function of temperature. An inset is shown to display the low temperature region

Spatially resolved magnetosome degradation at nanometer scale by nano-XRF and nano-XANES

To identify the subcellular location of the Fe phases we had observed with XANES, as well as identify the Fe phase of the small nanoparticles we had detected with TEM imaging, we used a combination of 2D XRF mapping and nano-XANES at the Hard X-Ray Nanoprobe (HXN) beamline at NSLS-II (USA). This method generates a stack of 2D nano-XRF maps at several energy points across the absorption edge and therefore each pixel contains a XANES spectrum. A detailed methodology can be found at Pattammattel et al. [46]. The spatial resolution of the method allows for the detection of additional Fe phases even if they are minoritary, as will be shown below.

We used sections of magnetosome loaded human lung carcinoma spheroids of 350 nm in width, at two time points of degradation: 2 hours (initial control) and 8 days (time point at which the small NPs observed with TEM had the biggest diameter and at which degradation was close to the maximum observed in XANES results). We mapped spheroid regions of up to 6×7 μm^2, with 50–100 nm/pixel resolution. Two representative XRF maps are shown in Fig. 5A-B.

We first analysed the XANES spectra of the entire XRF maps, fitting them to reference spectra of magnetite, maghemite and horse spleen ferritin (ferrihydrite) (Fig. 5C). At the 2 h time point, the spectra showed the best fit with just magnetite, as would be expected for magnetosomes that had just been internalized by the cells. Whereas after 8 days of degradation, the maps showed 25% of maghemite, indicating a clear oxidation of the magnetite. These results are similar to the ones obtained of XANES of entire spheroids, indicating that the XRF maps shown are representative of the full spheroids.

We then proceeded to analyse different regions from each map, by fitting the spectra of regions of interest (150×150 nm to 500×500 nm, see regions in Fig. 5A-B) to those of magnetite, maghemite and horse spleen ferritin. Examples of these spectra and fits are shown in Fig. 5D, and all analysed spectra and fits are shown in Figure S4.

At the 2 h time point, Fe-rich clusters were clearly visible, and the spectra from different regions of the clusters fitted with 100% magnetite, or in some cases, 90% magnetite and 10% maghemite (Fig. 5E). These results indicate that the observed clusters correspond to magnetosomes that have just been internalized by the cells. When contrast of the image was increased (see Fig. 5A zoom-in), no further Fe-rich clusters were visible in the background region.

At the 8-day degradation point, Fe-rich clusters were also visible, but unlike in the 2-hour maps, increasing the contrast of the image allowed to detect further Fe-rich clusters of lighter intensity (Fig. 5F). These results mirror those observed with TEM, with clusters of smaller nanoparticles rich in Fe appearing next to clusters of magnetosomes (Fig. 1A and D). Interestingly, fitting the spectra of representative regions of these clusters showcased differences in their composition, which allowed us to categorise them in two categories: clusters in which the best fit contained only magnetite and maghemite (which are numbered with the letter M); and clusters in which the best fit included horse spleen ferritin with a ferrihydrite core and hardly any maghemite (which are numbered with the letter F). To better showcase the difference between both types of clusters, a merge of clusters in each category is shown in Figure S5.

In M clusters, the best fits were obtained with magnetite ranging from 70 to 80%, and maghemite from 20 to 30%, indicating that the magnetite in magnetosomes was being oxidized to maghemite. These results are similar to those obtained from XANES of the entire spheroid, suggesting that these clusters are the predominant form of iron in the spheroids. F clusters, on the other hand, showed a best fit with magnetite (70–85%) and horse spleen ferritin (15–25%) (Fig. 5F). The lack of maghemite in most F clusters suggests that they may be newly synthesized magnetite, and not a direct product of magnetosome degradation. Furthermore, the fact that these clusters only appear in the 8 day sample, in combination with the presence of ferrihydrite in them, suggests that the magnetite detected in them is being synthesized by ferritin. The appearance of magnetite nanoparticles smaller than 10 nm (as would be expected of magnetic nanoparticles synthesized in ferritin's inner diameter cage) would explain the appearance of the peak in the derivative of the ZFC magnetisation curve at around 15 K (Fig. 4B).

Ferritin is well described to store iron in a ferrihydrite mineral core, although it is able to synthesize magnetic nanoparticles in vitro under specific circumstances, such as anaerobiosis, high temperatures (60–65 °C), and high pHs (8.5) [47]. The resulting magnetic protein is called magnetoferritin. While lung tumour spheroids have low oxygen concentration in their interior, it does not reach the anaerobiosis level (nor the high temperature or pH) employed for magnetoferritin synthesis in vitro. Our results suggest that ferritin is able to synthesize magnetite in human cells in a state of Fe excess, perhaps as protective measure against oxidative stress, as suggested by the overexpression of FTH1.

Magnetic iron oxide nanoparticles have previously been identified in human tissues: from brain tissue [48], to spleen, and cervical skin [49]. And their presence has often been linked to neurodegenerative diseases such as Alzheimer's disease [50, 51]. However the origin of these

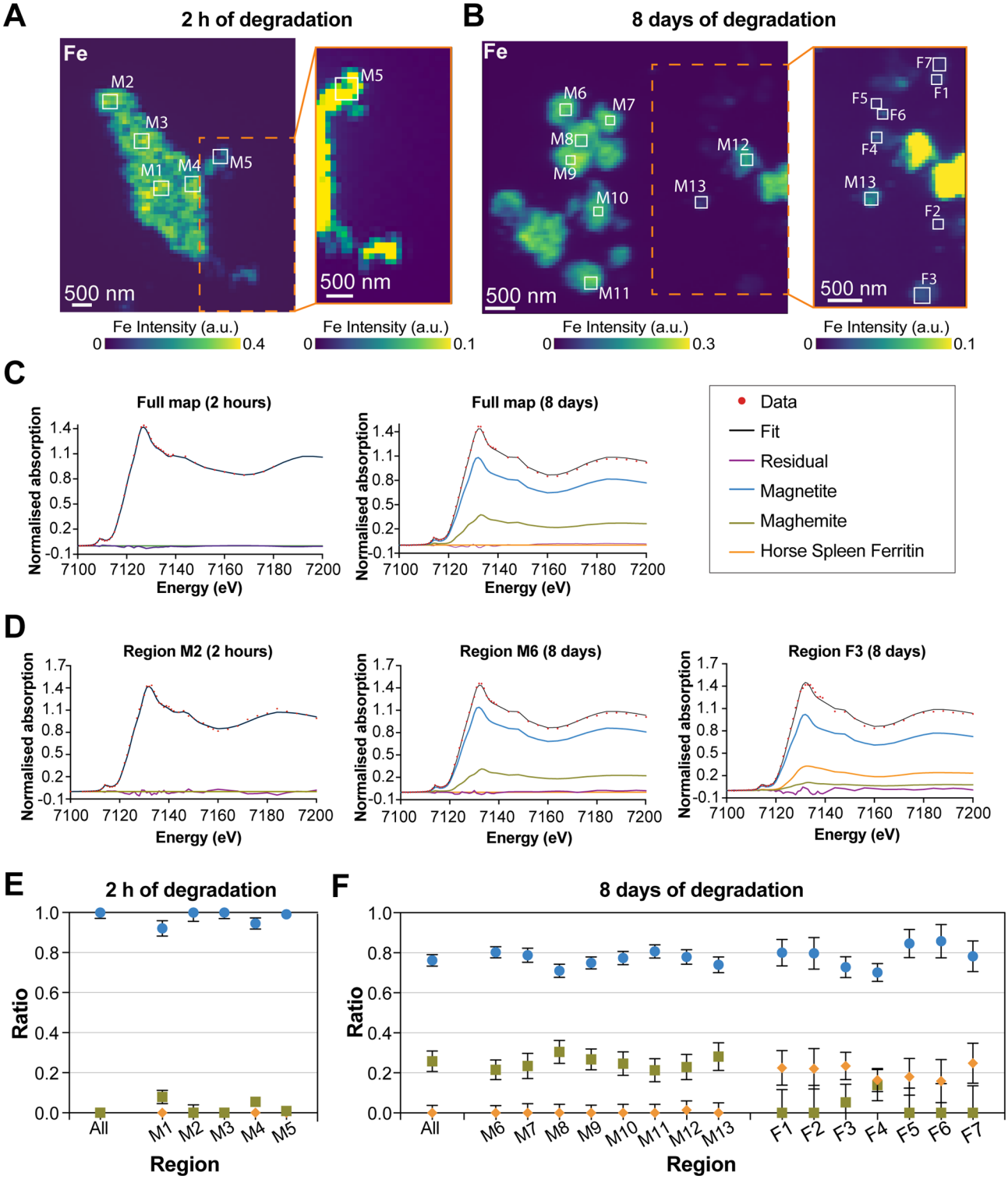

Fig. 5 **(A)** XRF map of Fe with 100 nm/px resolution, at 2 h after magnetosome internalisation in A549 cell spheroids. Regions of interest are marked with white squares. Intensity is shown in arbitrary units. A zoom-in of the selected are in shown with increased contrast. **(B)** XRF map of Fe with 50 nm/pixel resolution, at 8 days of magnetosome degradation in A549 cell spheroids. A zoom-in of the selected area is shown with increased contrast, to display all regions of interest, which are labelled as M or F depending on their composition. **(C)** Spectra for the entire XRF maps, and linear combination fit with magnetite, maghemite and horse spleen ferritin. **(D)** Spectra and linear combination fit for some of the regions highlighted in sections A and B. **E**-**F**. Results of fits with magnetite (blue), maghemite (green) and horse spleen ferritin with a ferrihydrite core (orange). Results are shown for the entire image (6 × 7 and 5 × 4 μm^2), as well as for all the regions of interest indicated in the XRF map

IONPs has long been disputed, and external pollution and contamination of the samples has often been demonstrated to be a source of the NPs [52–55]. Interestingly, Curcio et al. 2020 have reported that 2D mesenchymal stem cell cultures (but not 3D stem cell cultures nor human endothelial cells) are able to biosynthesize magnetite/maghemite during magnetite degradation, as they observe small nanoparticles with a magnetite/maghemite pattern in HR-TEM analysis [31]. Given their presence in 2D cell cultures but not spheroids, and in stem cells but not human endothelial cells, Curcio et al. hypothesized that magnetic nanoparticle biosynthesis was a phenomenon of 2D stem cell cultures. Our results suggest otherwise. Biosynthesis of magnetite might be a well established part of Fe metabolism, although the complex techniques required for detecting the small amounts of magnetite in the ferritin core could be the reason for it having been questioned for the last few decades. Furthermore, the process of nanoparticle biosynthesis in human cells in situations of high metal content might not be an iron specific phenomenon, as gold nanoparticles have also been shown to recrystallise following their degradation in human fibroblasts, in a process that is induced by ROS mediated oxidation of the NPs and might be stabilized by metallothionein proteins [56]. Biosynthesis of metal nanostructures in this context could be a protective mechanism against oxidative stress.

Conclusions

We have used nano-XRF and nano-XANES, combined with traditional methods such as transmission electron microscopy, analysis of gene expression, and magnetometry, to describe the degradation of magnetosomes in a human lung carcinoma model. We have observed two distinct processes: the degradation of the magnetite in magnetosomes, which is oxidized to maghemite, and the biosynthesis of small magnetite and ferrihydrite nanoparticles.

The degradation of magnetite, with its oxidation to maghemite and release of iron ions has previously been described in a few articles studying IONP degradation, both in cell culture [30] and in vitro simulating lysosomal conditions [57]. However the degradation rate and products are heavily dependent on the cell type and the type of cell culture employed (2D vs. 3D), highlighting the need for more biomimetic systems in biomedical research.

The biosynthesis of magnetic nanoparticles by cells, on the other hand, is not well understood. While magnetic nanoparticles of magnetite and maghemite have previously been observed in the human body, their origin has long been disputed. Our results suggest that biomineralisation of magnetite can occur in a 3D tumour model, and they support the hypothesis that ferritin can synthesize magnetite in human cells. Further studies will be required to understand how magnetite biomineralisation might play a role in iron metabolism and homeostasis.

As for the effect of our results on the biomedical prospects of magnetosomes, we believe the results here presented make magnetosomes interesting for treatments targeting solid tumours, as the high magnetisation level maintained by the spheroids (both due to their low degradation rate and their ability to biosynthesize magnetite) indicates low magnetosome dosages could be used for prolonged periods of time during treatment. Furthermore, patients with lung adenocarcinoma that accumulate iron in the tumour microenvironment have increased survival rates [58], suggesting that the presence of IONPs for a long time in a tumour could contribute to the treatment on its own.

Materials and methods

Magnetosome isolation

Magnetosomes were extracted from *M. gryphiswaldense* MSR-1 (DMSZ: DMS 6631). Magnetotactic bacteria were cultured in flask standard medium containing 100 µM of Fe(III) citrate [59]. For magnetosome extraction, bacteria were first collected by centrifugation at 8000 G (4ºC, 15 min), and resuspended in 20 mM HEPES −4 mM EDTA (pH 7.4). The collected bacteria were then disrupted using a French Press (GlenMills) at 1250 psig, this step was performed twice to ensure disruption of the bacteria. The lysate was then sonicated and washed three times with the following steps; first, magnetosomes were isolated in a magnetic rack, and rinsed with 10 mM HEPES-200 mM NaCl (pH 7.4). Then, the obtained suspension was sonicated at 40 W (45 cycles of 15" ON, 5" OFF) in an ice bath. After three rounds of magnetic rack separation and sonication, the magnetosomes were dispersed in 1 mL of HEPES 20 mM (pH 7.4), and stored with 3% glycerol at -80ºC. Before each use, magnetosomes were thawed and sonicated for 15 min in a water bath.

Cell culture

A549 cells (DSMZ: ACC 107) were cultured in Dulbecco's Modified Eagle's Medium/Nutrient Mixture F-12 Ham (DMEM/F-12, Sigma-Aldrich, D8900) supplemented with 2 mM L-glutamine, 10% fetal bovine serum (FBS, heat deactivated), 100 U/ml penicillin, 100 µg/mL streptomycin, and 0.25 µg/mL amphotericin B. Cells were cultured at 37ºC in a humidified atmosphere (95% relative humidity) and 5% CO_2.

Labelling cells with magnetosomes and spheroid formation

To label cells with magnetosomes, A549 cells in 6-well plates were incubated with magnetosomes for 2 h at a concentration of 30 µg/mL of magnetite, in DMEM/F-12

medium containing 5% FBS to prevent magnetosome aggregation. After 2 h, the culture medium was removed and replaced with fresh medium, in order to remove magnetosomes that were not attached to the cells, supplemented with 10% FBS.

For spheroid generation, A549 cells were collected by centrifugation (2 min, 2000 G). Cells were then diluted to the concentration of interest in DMEM/F-12 supplemented with 2 mM L-glutamine, 10% FBS, 100 U/mL penicillin, 100 µg/mL streptomycin, and 0.25 µg/mL amphotericin B. Cells were then seeded in 96-well low-adhesion U-bottom microplates for spheroid formation (ThermoScientific, Nuclon Sphera microplate). The media in the wells was changed to fresh DMEM/F-12 media every two-to-three days.

Cell viability assay

Cell viability was measured via ATP quantification with the Cell-Titer-GLO 3D Cell Viability Assay (Promega), luminescence was measured with a Synergy HT (Biotek) plate reader, in white Nunc A/S 96-well plates. Spheroids of 1×10^4 cells were used for the cell viability assays.

Sample preparation for electron microscopy, elemental mapping and electron diffraction analysis

For transmission electron microscopy (TEM) and elemental mapping/energy dispersive X-ray spectrometry (EDS) imaging, 1×10^4 cell spheroids were first washed with 0.1 M Sorensen's phosphate buffer (pH 7.4) to remove excess media, and fixed with 2% glutaradeldehyde overnight at 4ºC in the same buffer. Afterwards, cells were washed several times with isoosmolar phosphate/sucrose buffer, and dehydrated in increasing ethanol concentrations (from 30% up to 100%). The spheroids were then embedded in Epon Polarbed resin that polymerized at 55ºC for 48 h. A Leica UCT ultramicrotome with a Diatome diamond knife was used to obtain ultrathin sections of 70 nm thickness, which were then deposited onto carbon-coated copper grids.

Transmission electron microscopy (TEM)

TEM images were acquired in collaboration with the Analytic and High Resolution Microscopy in Biomedicine Service (SGIker), of the University of the Basque Country (UPV/EHU). Images were acquired with a JEOL JEM-1400 Plus electron microscope at an accelerating voltage of 120 kV. Size analysis of iron nanoparticles was performed using Fiji [60] .

Elemental mapping/energy dispersive X-ray spectrometry (EDS)

Element maps were obtained in collaboration with the Electronic Microscopy and Material Microanalysis Service (SGIker) of the University of the Basque Country (UPV/EHU). Transmission electron microscopy experiments were performed on a Talos F200i field emission gun instrument equipped with a Bruker X-Flash100 XEDS spectrometer.

Elemental maps were performed by XEDS in the STEM mode under high annular dark field (HAADF) detector for Z contrast imaging in STEM conditions (camera length of 160 mm) using a pixel size of 2 nm, a dwell time of 600 s and an image size of 512×512 pixels. Moreover, EDX microanalyses were carried out using a probe current of 120 pA and a semiconvergence angle of 6 mrad.

Selected area electron diffraction patterns (SAED) and HR-TEM

Selected Area Electron diffraction patterns (SAED) and high-resolution TEM images were obtained at Nanolab, University of Pannonia, using a Thermo Fisher Talos F200X electron microscope, operated at 200 kV accelerating voltage. Image processing, including the fast Fourier transformation (FFT) of HR-TEM images were performed using the Velox software.

X-ray absorption near-edge structure (XANES)

XANES experiments were performed at the Fe K-edge (7.112 keV) at the BM23 Beamline of the ESRF synchrotron (France). Four to five spheroids of 5×10^4 cells were combined for each XANES sample, to ensure enough Fe for analysis: spheroids were placed on Kapton tape, left to dry under infrared light and covered with another layer on Kapton foil on top. Samples were then measured in fluorescence mode at 10 K to avoid radiation damage. The monochromator was a double Si (111) crystal. XANES spectra were measured up to $k=9\ A^{-1}$, with a 0.2 eV step size at the edge region and 269 energy points. The energy was carefully calibrated by recording simultaneously a XANES spectrum of a Fe foil. Reference samples such as magnetosomes, maghemite and HoSF (Sigma-Aldrich, F7879) were measured in transmission configuration.

Data analysis was performed with the Athena program of the IFEFFIT package [61], using standard procedures for background subtraction and data normalisation. Linear combination fits to the aforementioned standards were also implemented in the Athena software. The goodness of the fits was evaluated by the R-factor [61]. R-factors for the fits were lower than 0.0005.

X-ray fluorescence microscopy (XRF) and nano-XANES

Samples were processed as for TEM experiments. A Leica UCT ultramicrotome with a glass blade was used to obtain thin sections of 350 nm thickness of 1×10^4 cell spheroids, which were then deposited onto Si_3N_4 membranes of 200 nm thickness (Norcada, NXCT-0101-Cr-1).

Scanning XRF maps were acquired at the Hard X-ray Nanoprobe (HXN) beamline at the National

Table 1 Primers employed for qRT-PCR experiment

Gen	Forward primer	Reverse primer
FTH1	GGCCGAATCTTCCTTCAGGATA	TGCACACTCCA TTGCATTCAG
FTL	TGTACCTGCAGGCCTCCTA	GCCTTCCAGAG CCACATCA
RPLP0	GCGACCTGGAAGTCCAAC	CACATTGTCTGC TCCCACAA
SLC40A1	GGGTGGACAAGAATGCTAGAC	CCACACAGGAT GACTGAAACA

Synchrotron Light Source II (NSLS-II) at Brookhaven National Laboratory. XRF maps were acquired at 7.2 keV. For nano-XANES data collection, XRF maps were collected across the Fe K-absorption edge at 7.112 keV using Fresnel Zone Plate (30 nm outer zone width) as nanofocusing optics. Detailed instrumentation of the beamline and data collection methods are reported here [46]. Briefly, XRF images were collected from 7.09 to 7.20 keV, with 60 energy points, a 1 eV step size at the edge region, at room temperature under 250 Torr He environment and with 0.05 s/pixel of exposure time per energy point. The incident energy was calibrated by measuring a Fe foil.

The data were acquired as follows: each pixel was irradiated 60 times, one for each energy point measured. The beam irradiated one pixel for 0.05 s, then moved on to the next pixel at the same energy, and so on until it measured the entire map at the desired energy. Once the entire map had been measured (>7.5 min for the XRF maps shown in this work), the beam returned to the initial pixel, and irradiated it at the next energy for another 0.05 s. The total time of irradiation for each pixel was of 3 s (0.05 s at a time, every>7.5 min).

After data acquisition, XRF maps were aligned with the ImageJ MultiStackReg plugging [62]. Images were analysed and the XANES spectra extracted using the XMIDAS software package [63]. XMIDAS package was used as well to remove background signal before spectra analysis. Linear combination fits were implemented in the Athena software [61]. R-factors for the fits were lower than 0.006.

RNA isolation and quantitative RT-PCR

Total RNA was isolated from 1×10^4 cell spheroids using the NZY Total RNA Isolation kit (NZY Tech), and eluted into 30 µL of double distilled H_2O. The total RNA extracted was then quantified using nanodrop, and the quality was checked by means of 28 S/18S ratio with LabChip GX Touch (Perkin Elmer), in combination with Standard RNA Reagent kit.

A combination of Biomark HD Nanofluidic qPCR System (Fluidigm) and FlexSix Dynamic Arrays IFC (IFC) were used for mRNA expression analysis. Firstly, DELTAGene Assays (Fluidigm) and pre-made PrimeTime qPCR Primer assays (IDT DNA Technologies) were used for mRNA detection, using an unspecific EvaGreen fluorochrome as reporter. cDNA synthesis was then performed with a NZY First-Strand cDNA synthesis Flexible pack (NZYTECH). 200 ng of RNA were added to a final reaction volume of 20 µL. A mix of random primers and oligo dTs were employed for cDNA synthesis. Three controls were included: additional samples for the qPCR standard curve (with 1000 ng RNA in 20 µL), RT-minus controls to check genomic DNA background in the sample (200 ng in 20 µL, without the RT enzyme), and the No Template control (NTC-ST) without RNA sample. The expression of genes RPLP0, PPIA and TBP was measured for their potential use as references, and RPLP0 was chosen as the reference gene for having the lowest variability of the three (Table 1).

Magnetometry

Magnetic measurements were performed with a superconducting quantum interference device magnetometer (SQUID, Quantum Design MPM3) in DC mode. Information on the saturation magnetisation of each sample (in emu) was acquired at 300 K, between −5000 and 5000 Oe. Each magnetometry measurement corresponds to one single spheroid.

For analysis in the SQUID magnetometer, spheroids were placed on Kapton foil, left to dry under infrared light and covered with another layer on Kapton foil on top. The sample was then placed in a straw for insertion into the magnetometer.

Inductively coupled plasma atomic emission spectroscopy (ICP/AES)

For iron quantification, four replicates were used for each time point analysed. Each replicate consisted of one spheroid digested in 300 µL of nitric acid at 80ºC and 100 µL of PBS (24 h, 80ºC). The digested solutions were then diluted 60x for analysis by ICP-AES (Agilent, 5110).

Statistical analysis

Graphical representation of data and statistical analysis were performed with GraphPad Prism 7.0. Gaussian distribution was tested with a D'Agostino-Person omnibus normality test. When the N value of a group was too low to run this normality test, non-parametric distribution was assumed. Unpaired t-test and Mann-Whitney tests were used when comparing two groups of data of parametric and non parametric distribution, respectively. Ordinary one-way ANOVAs and Kruskal-Wallis tests were employed to calculate significance of three or more groups of parametric and non-parametric distribution, respectively. $P<0.05$ (*), $P<0.01$ (**), and $P<0.001$ (***) were considered significant results.

Supplementary Information

The online version contains supplementary material available at https://doi.org/10.1186/s12951-024-02788-8.

Supplementary Material 1

Acknowledgements
This work was supported by grants PID2020-115704RB-C31 funded by the Spanish Ministerio de Ciencia, Innovación y Universidades (MCIN/AEI/10.13039/501100011033), and by IT1479-22 funded by the Basque Government. Electron microscopy performed at Nanolab, University of Pannonia was supported by the Hungarian National Research, Development and Innovation Office (NKFIH) under grant RRF-2.3.1-21-2022-00014. The authors thank SGIker (UPV/EHU/ERDF, EU) service for their technical and human support. Special thanks to Irene Fernández for her role in sample preparation for TEM and XRF experiments, Dr Ricardo Andrade for TEM imaging, Dr Ana Martínez for element mapping, and Dr Iñaki Orue for support with magnetometry measurements. We acknowledge the European Synchrotron Radiation Facility (ESRF) for provision of beamtime at BM23 beamline and we would like to thank Dr Thomas Buslaps and Dr Olivier Mathon for assistance and support. This research used resources HXN (3-ID) of the National Synchrotron Light Source II, a U.S. Department of Energy (DOE) Office of Science User Facility operated for the DOE Office of Science by Brookhaven National Laboratory under Contract No. DE-SC0012704.

Author contributions
AGG, AGP, AADC and MLFG conceptualised the project, experiments and analysis. AGG wrote the main manuscript. AGG generated and prepared experimental samples. All authors contributed in data acquisition, as here detailed: Fig. 1 (AGG, MP, MLFG), Fig. 2 (AGG, AADC), Fig. 3 (AGG, LG, AGP), Fig. 4 (AGG, AGP), Fig. 5 (AGG, LG, MLFG, AP), Supplementary Fig. 1 (AGG), Supplementary Fig. 2 (AGG), Supplementary Fig. 3 (AGG, AGP), Supplementary Fig. 4 (AGG, LG, MLFG, AGP), Supplementary Fig. 5 (AGG, LG, MLFG, AGP). AGG and AGP generated all figures. AGG, AGP, AADC and MLFG interpreted the data and edited the manuscript. All authors reviewed and approved the final manuscript.

Funding
This work was supported by grants PID2020-115704RB-C31 funded by the Spanish Ministerio de Ciencia, Innovación y Universidades (MCIN/AEI/10.13039/501100011033) , and by IT1479-22 funded by the Basque Government. Electron microscopy performed at Nanolab, University of Pannonia was supported by the Hungarian National Research, Development and Innovation Office (NKFIH) under grant RRF-2.3.1-21-2022-00014. This research used resources HXN (3-ID) of the National Synchrotron Light Source II, a U.S. Department of Energy (DOE) Office of Science User Facility operated for the DOE Office of Science by Brookhaven National Laboratory under Contract No. DE-SC0012704. European Synchrotron Radiation Facility (ESRF) provided beamtime at BM23 beamline.

Data availability
Data sets generated during the current study are available from the corresponding author on reasonable request.

Delcarations

Ethics approval and consent to participate
Not aplicable.

Consent for publication
Not aplicable.

Competing interests
The authors declare no competing interests.

Author details
[1]Department of Immunology, Microbiology and Parasitology, University of the Basque Country (UPV/EHU), Leioa 48940, Spain
[2]Bioscience and Biotechnology Institute of Aix-Marseille (BIAM), Aix-Marseille Université, CNRS, CEA-UMR 7265, Saint-Paul-les-Durance 13108, France
[3]Research Center of Biomolecular and Chemical Engineering, University of Pannonia Veszprém, Veszprém, Hungary
[4]HUN-REN-PE Environmental Mineralogy Research Group, Veszprém, Hungary
[5]National Synchrotron Light Source II, Brookhaven National Laboratory, Upton, NY 11973, USA
[6]Department of Electricity and Electronics, University of the Basque Country (UPV/EHU), Leioa 48940, Spain
[7]Department of Applied Physics, University of the Basque Country (UPV/EHU), Bilbao 48013, Spain

Received: 24 May 2024 / Accepted: 20 August 2024
Published online: 02 September 2024

References

1. Sung H, Ferlay J, Siegel RL, Laversanne M, Soerjomataram I, Jemal A, et al. Global Cancer statistics 2020: GLOBOCAN estimates of incidence and Mortality Worldwide for 36 cancers in 185 countries. CA Cancer J Clin. 2021;71(3):209–49.
2. Sharma A, Shambhwani D, Pandey S, Singh J, Lalhlenmawia H, Kumarasamy M, et al. Advances in Lung Cancer Treatment using Nanomedicines. ACS Omega. 2023;8(1):10–41.
3. Avasthi A, Caro C, Pozo-Torres E, Leal MP, García-Martín ML. Magnetic nanoparticles as MRI contrast agents. Top Curr Chem. 2020;378(3):40.
4. Zhuang D, Zhang H, Hu G, Guo B. Recent development of contrast agents for magnetic resonance and multimodal imaging of glioblastoma. J Nanobiotechnol. 2022;20(1):284.
5. Del Sol-Fernandez S, Martinez-Vicente P, Gomollon-Zueco P, Castro-Hinojosa C, Gutierrez L, Fratila RM, et al. Magnetogenetics: remote activation of cellular functions triggered by magnetic switches. Nanoscale. 2022;14(6):2091–118.
6. Van de Walle A, Figuerola A, Espinosa A, Abou-Hassan A, Estrader M, Wilhelm C. Emergence of magnetic nanoparticles in photothermal and ferroptotic therapies. Mater Horiz. 2023;10(11):4757–75.
7. Gavilan H, Simeonidis K, Myrovali E, Mazario E, Chubykalo-Fesenko O, Chantrell R, et al. How size, shape and assembly of magnetic nanoparticles give rise to different hyperthermia scenarios. Nanoscale. 2021;13(37):15631–46.
8. Sadhukha T, Wiedmann TS, Panyam J. Inhalable magnetic nanoparticles for targeted hyperthermia in lung cancer therapy. Biomaterials. 2013;34(21):5163–71.
9. Maier-Hauff K, Ulrich F, Nestler D, Niehoff H, Wust P, Thiesen B, et al. Efficacy and safety of intratumoral thermotherapy using magnetic iron-oxide nanoparticles combined with external beam radiotherapy on patients with recurrent glioblastoma multiforme. J Neurooncol. 2011;103(2):317–24.
10. Kok HP, Cressman ENK, Ceelen W, Brace CL, Ivkov R, Grull H, et al. Heating technology for malignant tumors: a review. Int J Hyperth. 2020;37(1):711–41.
11. NoCanTher. nocanther-project.eu. 2022.
12. Bazylinski DA, Frankel RB. Magnetosome formation in prokaryotes. Nat Rev Microbiol. 2004;2(3):217–30.
13. Fdez-Gubieda ML, Muela A, Alonso J, Garcia-Prieto A, Olivi L, Fernandez-Pacheco R, et al. Magnetite biomineralization in *Magnetospirillum gryphiswaldense*: time-resolved magnetic and structural studies. ACS Nano. 2013;7(4):3297–305.
14. Uebe R, Schuler D. Magnetosome biogenesis in magnetotactic bacteria. Nat Rev Microbiol. 2016;14(10):621–37.
15. Deng Q, Liu Y, Wang S, Xie M, Wu S, Chen A, et al. Construction of a Novel magnetic targeting Anti-tumor Drug Delivery System: Cytosine Arabinoside-loaded bacterial magnetosome. Mater (Basel). 2013;6(9):3755–63.
16. Erdal E, Demirbilek M, Yeh Y, Akbal Ö, Ruff L, Bozkurt D, et al. A comparative study of receptor-targeted magnetosome and HSA-Coated Iron oxide nanoparticles as MRI contrast-enhancing Agent in Animal Cancer Model. Appl Biochem Biotechnol. 2018;185(1):91–113.
17. Plan Sangnier A, Preveral S, Curcio A, A KAS, Lefèvre CT, Pignol D, et al. Targeted thermal therapy with genetically engineered magnetite magnetosomes@RGD: Photothermia is far more efficient than magnetic hyperthermia. J Control Release. 2018;279:271–81.
18. Tang Y-S, Wang D, Zhou C, Zhang S. Preparation and anti-tumor efficiency evaluation of bacterial magnetosome–anti-4-1BB antibody complex:

bacterial magnetosome as antibody carriers isolated from Magnetospirillum gryphiswaldense. Biotechnol Appl Chem. 2019;66(3):290–7.
19. Lefèvre CT, Bazylinski DA. Ecology, diversity, and evolution of magnetotactic bacteria. Microbiol Mol Biol Rev. 2013;77(3):497–526.
20. Alphandery E, Chebbi I, Guyot F, Durand-Dubief M. Use of bacterial magnetosomes in the magnetic hyperthermia treatment of tumours: a review. Int J Hyperther. 2013;29(8):801–9.
21. Muela A, Munoz D, Martin-Rodriguez R, Orue I, Garaio E, de Cerio AAD, et al. Optimal parameters for Hyperthermia Treatment using Biomineralized Magnetite nanoparticles: theoretical and experimental Approach. J Phys Chem C. 2016;120(42):24437–48.
22. Mickoleit F, Jorke C, Geimer S, Maier DS, Muller JP, Demut J, et al. Biocompatibility, uptake and subcellular localization of bacterial magnetosomes in mammalian cells. Nanoscale Adv. 2021;3(13):3799–815.
23. Nunes AS, Barros AS, Costa EC, Moreira AF, Correia IJ. 3D tumor spheroids as in vitro models to mimic in vivo human solid tumors resistance to therapeutic drugs. Biotechnol Bioeng. 2019;116(1):206–26.
24. Ma Pa, Xiao H, Yu C, Liu J, Cheng Z, Song H, et al. Enhanced cisplatin chemotherapy by Iron oxide nanocarrier-mediated generation of highly toxic reactive oxygen species. Nano Lett. 2017;17(2):928–37.
25. Feliu N, Docter D, Heine M, Del Pino P, Ashraf S, Kolosnjaj-Tabi J, et al. In vivo degeneration and the fate of inorganic nanoparticles. Chem Soc Rev. 2016;45(9):2440–57.
26. Nan X, Teng Y, Tian J, Hu Z, Fang Q. A comprehensive assessment of the biocompatibility of Magnetospirillum gryphiswaldense MSR-1 bacterial magnetosomes in vitro and in vivo. Toxicology. 2021;462:152949.
27. Zelepukin IV, Yaremenko AV, Ivanov IN, Yuryev MV, Cherkasov VR, Deyev SM, et al. Long-term fate of magnetic particles in mice: a Comprehensive Study. ACS Nano. 2021;15(7):11341–57.
28. Portilla Y, Fernández-Afonso Y, Pérez-Yagüe S, Mulens-Arias V, Morales MP, Gutiérrez L, et al. Different coatings on magnetic nanoparticles dictate their degradation kinetics in vivo for 15 months after intravenous administration in mice. J Nanobiotechnol. 2022;20(1):543.
29. Alphandery E, Idbaih A, Adam C, Delattre JY, Schmitt C, Gazeau F, et al. Biodegraded magnetosomes with reduced size and heating power maintain a persistent activity against intracranial U87-Luc mouse GBM tumors. J Nanobiotechnol. 2019;17(1):126.
30. Gandarias L, Gubieda AG, Gorni G, Mathon O, Olivi L, Abad-Diaz-de-Cerio A, et al. Intracellular transformation and disposal mechanisms of magnetosomes in macrophages and cancer cells. Biotechnol J. 2023;18(10):e2300173.
31. Curcio A, Van de Walle A, Serrano A, Preveral S, Pechoux C, Pignol D, et al. Transformation cycle of magnetosomes in Human Stem cells: from degradation to biosynthesis of magnetic nanoparticles anew. ACS Nano. 2020;14(2):1406–17.
32. Lavorato M, Franzini-Armstrong C. Practical Solutions to frequent problems encountered in thin sections Electron Microscopy. Microscopy Today. 2017;25(3):40–5.
33. Cypriano J, Werckmann J, Vargas G, Lopes Dos Santos A, Silva KT, Leao P, et al. Uptake and persistence of bacterial magnetite magnetosomes in a mammalian cell line: implications for medical and biotechnological applications. PLoS ONE. 2019;14(4):e0215657.
34. Van de Walle A, Plan Sangnier A, Abou-Hassan A, Curcio A, Hemadi M, Menguy N, et al. Biosynthesis of magnetic nanoparticles from nano-degradation products revealed in human stem cells. Proc Natl Acad Sci U S A. 2019;116(10):4044–53.
35. Plays M, Muller S, Rodriguez R. Chemistry and biology of ferritin. Metallomics. 2021;13(5).
36. Drits VA, Sakharov BA, Salyn AL, Manceau A. Structural model for Ferrihydrite. Clay Miner. 1993;28:185–207.
37. Lawson DM, Treffry A, Artymiuk PJ, Harrison PM, Yewdall SJ, Luzzago A, et al. Identification of the ferroxidase centre in ferritin. FEBS Lett. 1989;254(1–2):207–10.
38. Wang S, Luo J, Zhang Z, Dong D, Shen Y, Fang Y, et al. Iron and magnetic: new research direction of the ferroptosis-based cancer therapy. Am J Cancer Res. 2018;8(10):1933–46.
39. Zhang N, Yu X, Xie J, Xu H. New insights into the role of Ferritin in Iron Homeostasis and neurodegenerative diseases. Mol Neurobiol. 2021;58(6):2812–23.
40. Mehlenbacher M, Poli M, Arosio P, Santambrogio P, Levi S, Chasteen ND, et al. Iron oxidation and core formation in recombinant Heteropolymeric Human ferritins. Biochemistry. 2017;56(30):3900–12.
41. Donovan A, Brownlie A, Zhou Y, Shepard J, Pratt SJ, Moynihan J, et al. Positional cloning of zebrafish ferroportin1 identifies a conserved vertebrate iron exporter. Nature. 2000;403(6771):776–81.
42. Cohen LA, Gutierrez L, Weiss A, Leichtmann-Bardoogo Y, Zhang DL, Crooks DR, et al. Serum ferritin is derived primarily from macrophages through a nonclassical secretory pathway. Blood. 2010;116(9):1574–84.
43. Kimura T, Jia J, Kumar S, Choi SW, Gu Y, Mudd M, et al. Dedicated SNAREs and specialized TRIM cargo receptors mediate secretory autophagy. EMBO J. 2017;36(1):42–60.
44. Battaglia AM, Sacco A, Vecchio E, Scicchitano S, Petriaggi L, Giorgio E, et al. Iron affects the sphere-forming ability of ovarian cancer cells in non-adherent culture conditions. Front Cell Dev Biol. 2023;11:1272667.
45. Marcano L, Garcia-Prieto A, Munoz D, Fernandez Barquin L, Orue I, Alonso J, et al. Influence of the bacterial growth phase on the magnetic properties of magnetosomes synthesized by *Magnetospirillum gryphiswaldense*. Biochim Biophys Acta Gen Subj. 2017;1861(6):1507–14.
46. Pattammattel A, Tappero R, Ge M, Chu YS, Huang X, Gao Y et al. High-sensitivity nanoscale chemical imaging with hard x-ray nano-XANES. Sci Adv. 2020;6(37).
47. Meldrum FC, Heywood BR, Mann S. Magnetoferritin: in vitro synthesis of a novel magnetic protein. Science. 1992;257(5069):522–3.
48. Kirschvink JL, Kobayashi-Kirschvink A, Woodford BJ. Magnetite biomineralization in the human brain. Proc Natl Acad Sci U S A. 1992;89(16):7683–7.
49. Murros K, Wasiljeff J, Macias-Sanchez E, Faivre D, Soinne L, Valtonen J, et al. Magnetic nanoparticles in human cervical skin. Front Med (Lausanne). 2019;6:123.
50. Hautot D, Pankhurst QA, Khan N, Dobson J. Preliminary evaluation of nanoscale biogenic magnetite in Alzheimer's disease brain tissue. Proc Biol Sci. 2003;270(Suppl 1Suppl 1):S62–4.
51. Pankhurst Q, Hautot D, Khan N, Dobson J. Increased levels of magnetic iron compounds in Alzheimer's disease. J Alzheimers Dis. 2008;13(1):49–52.
52. Maher BA, Ahmed IA, Karloukovski V, MacLaren DA, Foulds PG, Allsop D, et al. Magnetite pollution nanoparticles in the human brain. Proc Natl Acad Sci U S A. 2016;113(39):10797–801.
53. Calderon-Garciduenas L, Gonzalez-Maciel A, Mukherjee PS, Reynoso-Robles R, Perez-Guille B, Gayosso-Chavez C, et al. Combustion- and friction-derived magnetic air pollution nanoparticles in human hearts. Environ Res. 2019;176:108567.
54. Lu D, Luo Q, Chen R, Zhuansun Y, Jiang J, Wang W, et al. Chemical multi-fingerprinting of exogenous ultrafine particles in human serum and pleural effusion. Nat Commun. 2020;11(1):2567.
55. Hammond J, Maher BA, Ahmed IAM, Allsop D. Variation in the concentration and regional distribution of magnetic nanoparticles in human brains, with and without Alzheimer's disease, from the UK. Sci Rep. 2021;11(1):9363.
56. Balfourier A, Luciani N, Wang G, Lelong G, Ersen O, Khelfa A, et al. Unexpected intracellular biodegradation and recrystallization of gold nanoparticles. Proc Natl Acad Sci U S A. 2020;117(1):103–13.
57. Gutierrez L, Romero S, da Silva GB, Costo R, Vargas MD, Ronconi CM, et al. Degradation of magnetic nanoparticles mimicking lysosomal conditions followed by AC susceptibility. Biomed Tech (Berl). 2015;60(5):417–25.
58. Thielmann CM, Costa da Silva M, Muley T, Meister M, Herpel E, Muckenthaler MU. Iron accumulation in tumor-associated macrophages marks an improved overall survival in patients with lung adenocarcinoma. Sci Rep. 2019;9(1):11326.
59. Heyen U, Schuler D. Growth and magnetosome formation by microaerophilic Magnetospirillum strains in an oxygen-controlled fermentor. Appl Microbiol Biotechnol. 2003;61(5–6):536–44.
60. Schindelin J, Arganda-Carreras I, Frise E, Kaynig V, Longair M, Pietzsch T, et al. Fiji: an open-source platform for biological-image analysis. Nat Methods. 2012;9(7):676–82.
61. Ravel B, Newville M. ATHENA, ARTEMIS, HEPHAESTUS: data analysis for X-ray absorption spectroscopy using IFEFFIT. J Synchrotron Radiat. 2005;12(Pt 4):537–41.
62. Thevenaz P, Ruttimann UE, Unser M. A pyramid approach to subpixel registration based on intensity. IEEE Trans Image Process. 1998;7(1):27–41.
63. Pattammattel A, Tappero R, Gavrilov D, Zhang H, Aronstein P, Forman HJ et al. Multimodal X-ray nano-spectromicroscopy analysis of chemically heterogeneous systems. Metallomics. 2022;14(10).

Publisher's note